Supporting Information

High quantum efficiency nanopillar photodiodes overcoming the diffraction limit of light

Wook-Jae Lee1[1,‖,*], *Pradeep Senanayake*[1,‖], *Alan C. Farrell*[1], *Andrew Lin*[1], *Chung-Hong Hung*[2] *& Diana. L. Huffaker*[1,3]

[1]Department of Electrical Engineering, University of California Los Angeles, Los Angeles, California 90095, United States

[2]Nanopixel Technologies LLC, Los Angeles, California 90095, United States

[3]California Nano-Systems Institute, University of California Los Angeles, Los Angeles, California 90095, United States

KEYWORDS

Nanowires, nanopillar, InAsSb, nanophotodiode, diffraction limit, surface plasmons

Methods

InAsSb nanopillar growth. InAsSb nanopillars were grown on a p-doped InAs buffer layer on GaAs (111)B substrates via catalyst-free, selective-area epitaxy using metal-organic chemical vapor deposition (MOCVD). Trimethylindium (TMIn), tertiarybutylarsine (TBAs) and trisdimethylaminoantimony (TDMASb) were used as precursors. The SiO_2 (20-nm thick) growth mask is defined into 200 μm square arrays of nanoholes with a opening of 160 nm and a pitch of 900 nm by e-beam lithography and reactive ion etching. The growth pressure and temperature were 60 torr and 560 °C, respectively. The gas-phase TDMASb composition ([TDMASb] / ([TDMASb] + [TBA])) was 40% corresponding to $InAs_{0.93}Sb_{0.07}$.[1] The height and diameter of NPs are highly depend on array pitch where increasing the pitch results in shorter heights and larger diameters.

NP PDs fabrication. The Cr/Au (10 nm/150 nm) bottom contact is deposited by electron-beam evaporation (CHA Solution) on InAs buffer layer. The NP arrays is planarized using the bisbenzocyclobutene (BCB, CYCLOTENE, Dow Chemical) and hard cured at 250°C for 60 minute. The BCB layer is etched back to reveal the NP tips (~ 500 nm) by Oxford 80 Plus reactive ion etcher (RIE) and the Cr/Au (10 nm/150 nm) top contact is evaporated with the substrate mounted at an angle to expose a self-aligned nanohole array.

Finite-difference time-domain simulations. We performed the numerical calculation on the absorption in NPs by using a commercial-grade simulator based on finite-difference time-domain (FDTD) method (Lumerical, FDTD Solutions). The refractive index of NPs was taken from Palik data[2]. A three-dimensional discretization mesh was 7 nm × 7 nm × 11 nm employed. Periodic boundary conditions and bloch boundary conditions are applied in *x*- and *y*-directions

for normal angle of incidence and 16° angle of incidence, respectively, while perfectly matched layer absorbing boundary condition is used in the *z*-direction.

Experimental set-up. The fabricated NP PDs sample mounted in a cryostat was cooled down by liquid nitrogen. The optical spectra were observed by using a Fourier-transform infrared (FTIR) spectrometer (Thermo Scientific Nicolet 6700) attached to an infrared microscope (Thermo Scientific Nicolet Continuμm) equipped with the mounted NP PDs . FTIR data is collected in the spectral range 2000-10000 cm^{-1} with 4 cm^{-1} resolution and averaging of 32 scans. IR source light with 150 μm × 150 μm area was focused through a 15× Reflachromat Objective (N.A. 0.58) coupled with side port reflectance accessory.

Detailed fabrication process

We employed p-doped InAs buffer layer through optimizing molecular beam epitaxy (MBE) growth on GaAs (111)B substrates - promising low cost manufacturing - in order to grow InAsSb NPs. Figure S1 shows material characterization of InAs buffer layers on GaAs (111)B substrates. Figure S1a,b show atomic force microscope (AFM) images of InAs grown at 400^{o}C and 450 ^{o}C, respectively. Pyramidal faceting can be observed on both surfaces. The surface of the InAs buffer layer becomes smoother at 450 ^{o}C, with a reduction in root mean square (RMS) roughness to 2.34nm. However, pits in the surface are also observed. This study shows that there is a tradeoff between pyramidal surfaces and pit density. The InAs surface produced at a growth temperature of 450 ^{o}C and As flux 110 mil was considered sufficiently smooth for nanopillar epitaxy. Figure S1c shows a cross-sectional transmission electron microscopy (TEM) image of the InAs/GaAs interface. The InAs/GaAs system is a highly lattice mismatched, with a lattice mismatch of 7.2%. Typically, a strain induced 2D-3D morphological transition takes place known as SK growth mode, where the strain is relieved by the formations of islands. However, in the growth of InAs on GaAs (111) B these highly lattice mismatched systems are forced to grow in a 2D mode where strain relief takes place via a regular array of Lomer misfit dislocations and can be seen at the interface. The presence of a regular array of misfit dislocations is highly advantageous for the realization of bandgap engineered epitaxy.

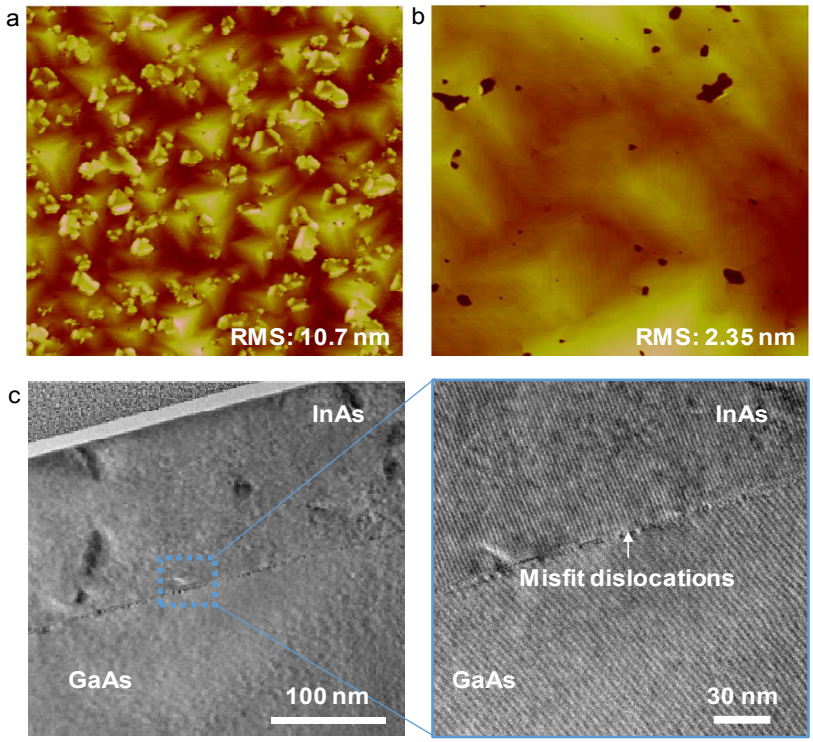

Figure S1. AFM images in a 10 x 10 µm scan area of the MBE grown InAs epi-layer on GaAs (111)B at a growth temperature of (a) 400 ^{o}C and As flux 110 mil , and (b) 450 ^{o}C and As flux 110 mil. (c) Cross sectional TEM image of InAs epi-layer and high resolution TEM image showing misfit dislocation.

The schematics of detailed fabrication process after MBE growth are shown in Fig. S2. SiO_2 of 20 nm thickness is deposited via electron-beam evaporation (CHA Solution) and nanoholes of 160 nm diameter and 900 nm pitch are defined into 200 µm square arrays through reactive ion etching. The NP arrays are grown under pressure and temperature of 60 torr and 560 °C, respectively. The NP arrays are then planarized for electric isolation using bisbenzocyclobutene (BCB, CYCLOTENE, Dow Chemical) and hard cured at 250°C for 60 minutes in a Carbolite high temperature oven. The bottom contact (Cr 10nm/Au 150 nm) is deposited by electron-beam evaporation (CHA Solution) on the InAs buffer layer. The top contact (Cr 10nm/Au 150 nm) is evaporated with the substrate mounted at an angle after etch-back of the BCB layer by Oxford 80 Plus reactive ion etcher.

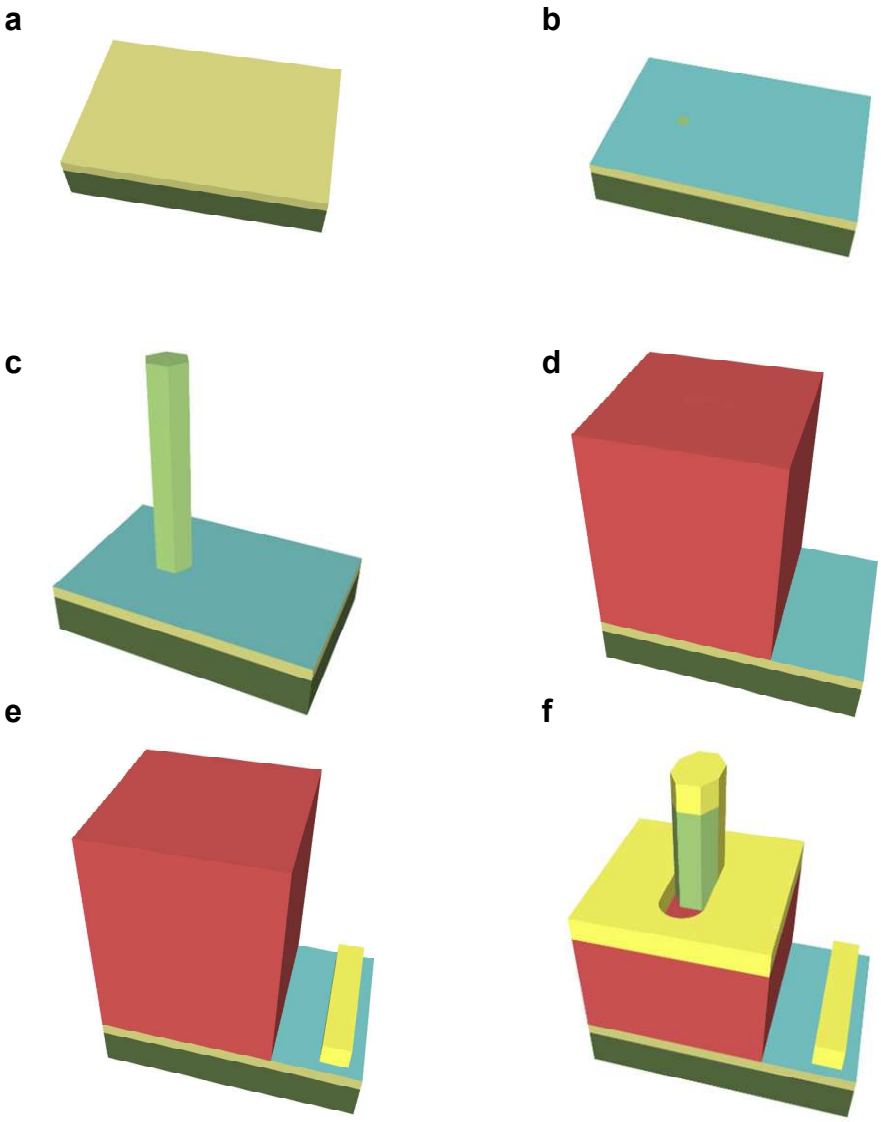

Figure S2. Schematic representation of the fabrication process of the nanopillar photodiode with partially covered metal. (a) InAs buffer layer growth of a 200 nm thickness on GaAs (111)B substrate by MBE. (b) Hole patterning in SiO2 mask layer with a 20 nm mask layer for selectrive area epitaxy using metal-organic chemical vapor deposition (MOCVD). (c) InAsSb nanopillar growth by MOCVD. (d) BCB polymer planarization for electrical isolation. (e) Deposition of the bottom contact. (f) BCB etch back and the tilted deposition of the top contact.

Experimental setup and responsivity measurement

The experimental setup is shown in Fig. S3. The wire-bonded NP PD sample was cooled with liquid nitrogen in a cryostat. The optical spectra were analyzed by a Fourier-transform infrared (FTIR) spectrometer (Thermo Scientific Nicolet 6700) equipped with an infrared microscope (Thermo Scientific Nicolet Continuμm). The NP PDs were illuminated by a thermal IR emitter passing through the FTIR and the light was focused in 150 μm × 150 μm area by a 15× Reflachromat Objective coupled with side port reflectance accessory. The photocurrent spectra were then collected in rapid scan mode with a spectral resolution of 4 cm^{-1} in the spectral range 2000-10000 cm^{-1} and averaging of 32 scans.

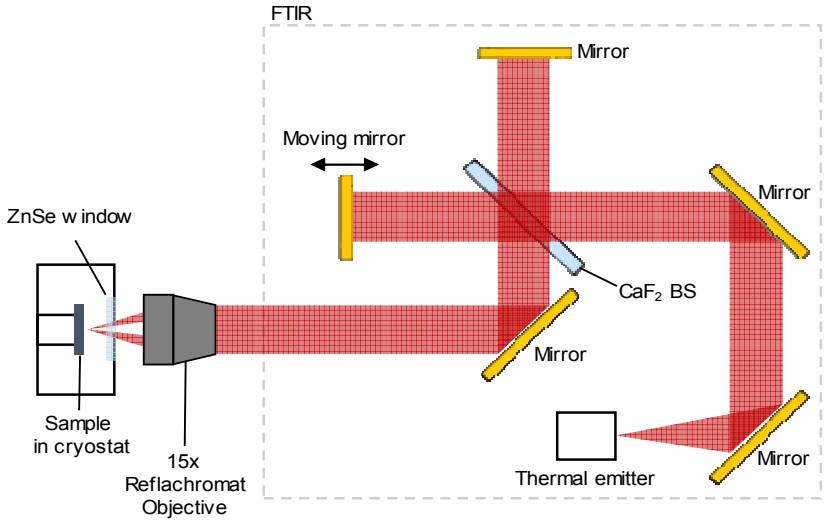

Figure S3. Experimental setup for measuring the responsivity of NP PDs. BS indicates beam splitter.

Figure S4 shows how the responsivity can be obtained by taking advantage of the different responses of the DTGS detector with regards to various mirror velocities in the FTIR. We start by assuming that the DTGS detector shows a flat spectral response, which means the response proportional to the incident light power at each wavelength, as opposed to a semiconductor detector. However, the spectral response of the DTGS depends on optics in the FTIR, such as the interferometer mirror velocity. In order to compensate the spectral response of the DTGS, the

responses of the DTGS at various mirror velocities and a few fixed wavelengths are measured as a function of wavenumber, as depicted in Fig. S4a. It is shown that there is a decrease of the response at shorter wavelengths (that is, large wavenumber) due to an underestimation of the light source by high frequency roll-off. We chose the response of the DTGS at 1.5 μm wavelength. The response at any arbitrary frequency can be extracted by fitting the measured response with a characteristic response equation and then the response of the DTGS is compensated as shown in Fig. S4b. The calibrated responses of a commercial InGaAs detector (Global Communication Semiconductor) and our NP PDs divided by the compensated response of the DTGS are plotted in Fig. S4c and d, respectively. Finally, the arbitrary responsivity is converted to units of amperes per watt by multiplying by a calibrated commercial InGaAs detector responsivity.

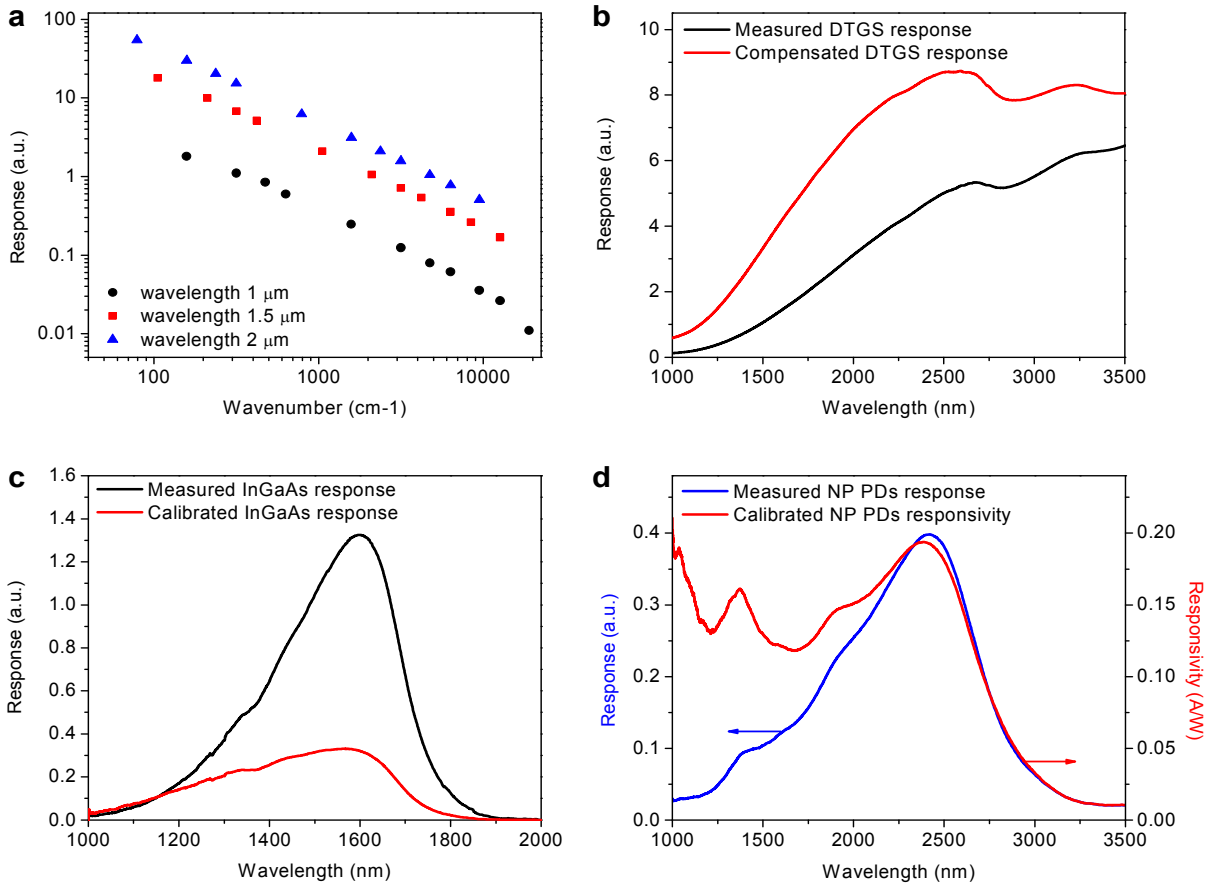

Figure S4. Responsivity measurement and unit conversion. (a) Measured frequency response of DTGS at various wavelengths in terms of the mirror velocity in the FTIR. (b) Comparison of the measured response with the compensated response of DTGS by taking advantage of a different magnitude at different mirror velocities. (c) Calibration of a commercial InGaAs detector response with the responsivity of 0.9 A/W at 1310 nm given by dividing by the compensated response of DTGS. (d) Calibration of InAsSb NP PDs response given by dividing by the compensated response of DTGS. The arbitrary units of the InAsSb NP PDs response (blue curve, left axis) are divided by the response and multiplied by the responsivity of the commercial InGaAs detector in order to convert to units of amperes per watt (red curve, right axis).

InAs buffer layer contribution to the photocurrent

Figure S5 shows the calculated absorption behaviors for the InAs film of 200 nm thickness and the proposed NP structure with different polarization of incident light. The absorption for the InAs film of 200 nm thickness continually decreases with increasing the wavelength of incident light due to its absorption coefficient. Thus, the absorption behavior does not match with our results. We also confirmed that the spectral response disappears when light is incident on nanowires which are not covered by metal. These mean that the InAs buffer layer does not contribute to the photocurrent.

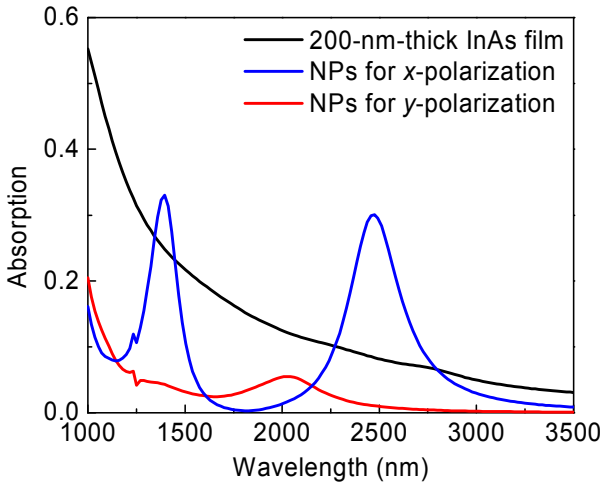

Figure S5. Calculated absorption for the InAs film and proposed nanowire structure with different polarization of incident light.

Angle of incidence of a reflective objective

The IR light in this experiment was focused by a reflective objective (15× Reflachromat Objective, N.A. 0.58) with achromatic behavior over a broad wavelength range. The central area of the focused light is blocked by the mirror of the reflective objective, resulting in a doughnut-shaped beam with an inner angle of 16° and outer angle of 35.5°, as shown in Fig S6a. In order to investigate the effect of different angles of incidence of IR light, we show the calculated absorption in NP PDs at 20° and 30° in Fig S6b and c, respectively. The overall profiles and the locations of the peaks of the absorption are very similar to each other, including at 16°, except that the absorption of *x*-polarization is increased as the angle of incidence is increased. It is clear that the measured spectral response is the averaged absorption over the angle of incidence range and the enhanced absorption of *x*-polarization at large angles improves the responsivity near 2,000 nm.

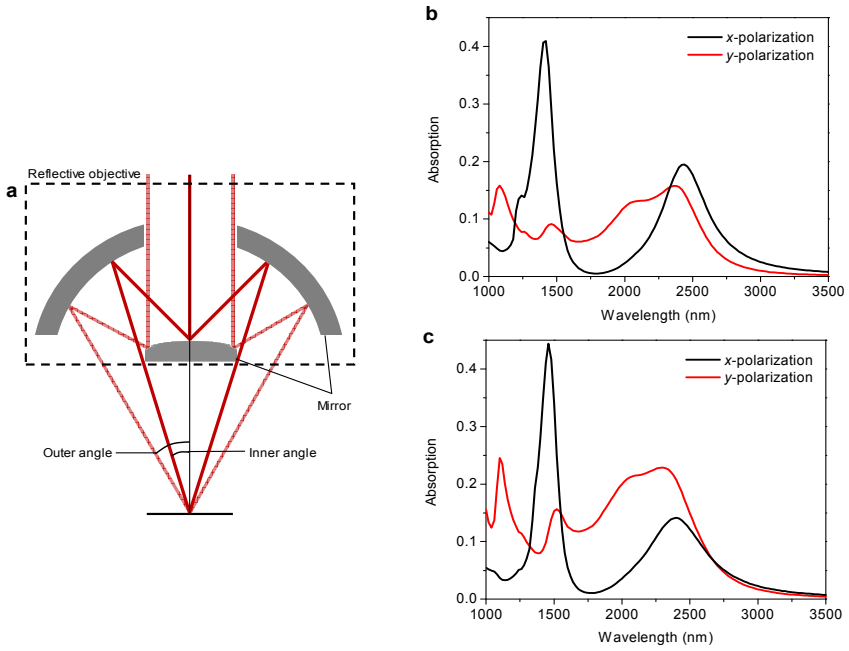

Figure S6. (a) Schematic diagram of a focusing light through a reflective objective. Calculated absorption in NP PDs at the angles of incidence of (b) 20° and (c) 30°.

Role of NP period

An increase in the period of NP leads to a redshift of the localized surface plasmon (LSP) resonances.[3–6] Figure S7 shows the calculated absorption behaviors of proposed plasmonic NPs with various periods under x-, y-polarized and normal incident illumination. In the case of our NPs, it is clearly indicated that the absorption peaks due to the LSP resonances are red-shifted although the wavelength of the absorption peak is not much changed for y-polarized light because the LSP resonance wavelength is affected by the distance between NPs. The LSP resonance wavelength shifts depending on the period (short-range interactions for short period NPs and long-range interactions for long period NPs). The LSPs can be strongly coupled to each other with decreasing the period of NPs (LSP resonances around 2500 nm for x-polarized light), but in our case we have to consider how much the LSPs can be absorbed in NPs (LSP resonances around 1500 nm for x-polarized light).

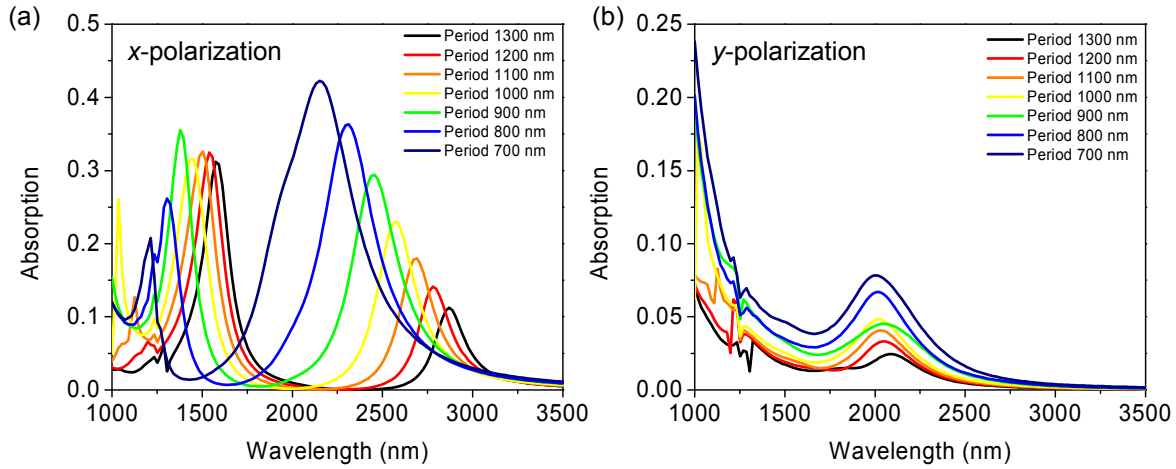

Figure S7. Calculated absorption behaviors of proposed plasmonic NPs with various periods for (a) *x*-polarized and (b) *y*-polarized light under normal incident illumination.

Response comparison of NP PDs with commercial InSb detector

Figure S8 shows the measured responses of commercial InSb detector (Thermo Scientific) and our NP PDs. Although our NP PDs cannot compete with planar PDs in terms of responsivity, they can compete in terms of cost. In order for planar PDs to achieve this responsivity, very thick absorption layers are required. Furthermore, in order to achieve low dark current, lattice-matched substrates are required. These two requirements result in very high cost. Our NP PDs can be grown on low-cost GaAs substrates with InAs epi-layer (or potentially directly on silicon substrates) and NPs require only a small fraction of the material required for planar growth.

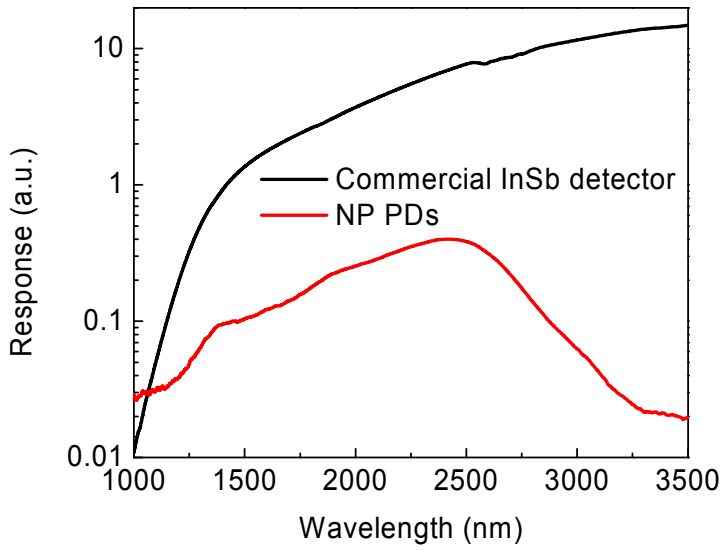

Figure S8. Measured responses of commercial InSb detector (Thermo Scientific) and NP PDs as a function of wavelength at 77 K.

REFERENCES

1. Farrell, A. C. *et al.* High-Quality InAsSb Nanowires Grown by Catalyst-Free Selective-Area Metal–Organic Chemical Vapor Deposition. *Nano Lett.* **15,** 6614–6619 (2015).

2. Palik, E. D. *Handbook of Optical Constants of Solids*. (Academic, 1985).

3. Zhao, L. *et al.* The extinction spectra of silver nanoparticle arrays: Influence of array structure on plasmon resonance wavelength and width. *J. Phys. Chem. B* **107,** 7343–7350 (2003).

4. Byun, K. M., Kim, S. J. & Kim, D. Profile effect on the feasibility of extinction-based localized surface plasmon resonance biosensors with metallic nanowires. *Appl. Opt.* **45,** 3382–9 (2006).

5. Parsons, J. *et al.* Localized surface-plasmon resonances in periodic nondiffracting metallic nanoparticle and nanohole arrays. *Phys. Rev. B* **79,** 073412 (2009).

6. Du, L., Zhang, X., Mei, T. & Yuan, X. Localized surface plasmons, surface plasmon polaritons, and their coupling in 2D metallic array for SERS. *Opt. Express* **18,** 1959–1965 (2010).